A Probability-Based Daytime Algorithm for Sea Fog Detection Using GOES-16 Imagery

Sahel Mahdavi [ID], Meisam Amani [ID], *Senior Member, IEEE*, Terry Bullock, and Steven Beale

Abstract—Fog is a hazardous weather event that can endanger navigation, aviation, and transportation. While human has several limitations in detecting and forecasting offshore fog, satellite remote sensing offers cost-effective images. In this study, a probability-based daytime sea fog detection algorithm, applied to geostationary operational environmental satellite (GOES) 16 satellite data over the Grand Banks offshore Eastern Canada, is presented and compared with the National Oceanographic and Atmospheric Administration (NOAA)'s Low Instrument Flight Rules (LIFR) probability map. Initially, clear-sky and ice cloud classes were delineated in the GOES-16 image and then the remaining pixels were assigned a fog probability by conducting small droplet proxy, spatial homogeneity, and temperature difference tests. Moreover, a green band was linearly interpolated using the first three bands of GOES-16 images to generate pseudotrue color composites. The resulting maps were evaluated both during an extended sea fog event and using several statistical measures. The average detection probability for the observed advection fog events was 66% for the proposed method, while that for NOAA's LIFR map was 38%. Furthermore, by thresholding the generated maps at the probability of 60%, the false alarm rate, probability of detection, hit rate, and Hanssen–Kuiper skill score were 0.09, 0.77, 0.83, and 0.68, respectively. The proposed method is operationally being used in this region to detect and monitor sea fog, facilitating safe navigation and aviation. This is the first study that uses GOES-16 for daytime fog detection and discusses a satellite-based solution for fog modeling in Grand Banks, NL.

Index Terms—Geostationary operational environmental satellite (GOES) 16, grand banks, remote sensing (RS), sea fog.

I. INTRODUCTION

FOG is a hazardous weather phenomenon that appears when water vapor near the surface is condensed to form suspended water droplets [1]. Fog can impose serious dangers to navigation, aviation, and transportation as it can reduce the horizontal visibility to below 1 km, which in turn can affect the economy and endanger lives [2]–[5]. In fact, the amount of economic loss incurred by fog is comparable to that of tornados

and hurricanes [6]. Consequently, nowcasting and forecasting this phenomenon over oceans are crucial for safe navigation and aviation [7] but are still associated with several technical problems [4].

In the case of marine fog, human-recorded observations cover only a limited area over a short period of time, ground stations for marine fog detection are sparse, and numerical weather prediction models usually do not provide high accuracy unless a dense set of observations is available, which is usually not the case over the oceans [5], [8]. However, earth observation (EO) satellites offer cost-effective and timely images for covering large areas (even the whole globe) with a reasonable spatial resolution and temporal frequency [9] and provide valuable information regarding the extent and distribution of different meteorological phenomena [10]–[12]. However, daytime sea fog detection is more challenging because of the similarity in the spectral characteristics of fog, snow, and other types of cloud, and the effect of solar radiation on the 3.9 μm band [4], [5], [8]. In the nighttime, using the 3.9 μm band is more useful because of the similarity between the wavelength of this band and the mean droplet size of fog [13].

Based upon the above discussion, several studies, dating back to as early as the 1970s, have attempted to identify sea fog using remotely sensed satellite imagery [14]. One common approach for this purpose is thresholding a satellite image that has been applied in several studies. For example, Deng *et al.* [2] detected low cloud and fog by thresholding and comparing several bands of moderate-resolution imaging spectroradiometer (MODIS) and validated it using the sea fog observations from the coastal regions. However, using a fixed threshold might be inaccurate, as usually, the threshold values change diurnally and seasonally [5], [15]. The dynamic thresholds can fix this issue to some extent. For instance, a general method was introduced in [3] in which the thresholds for detecting sea fog and eliminating medium and high clouds were determined dynamically. The approach was verified using the visibility observations in the study area and can be implemented using any sensor having at least one visible and one thermal channel.

Considering the difference between the brightness temperature of clouds and clear sky or between two bands of a satellite sensor is another method for sea fog and low stratus (FLS) detection. For instance, Zhang and Yi [9] identified FLS based on the difference between the brightness temperature at the top of the clouds and sea surface temperature (SST) using MODIS imagery and month-dependent thresholds. In [5], other than the difference between 3.9 and 11.2 μm channels, which

is commonly used in sea fog detection studies, several other metrics were applied to MODIS data, including the brightness temperature difference between the clear sky and nearby clouds, and the normalized difference water vapor index. Similarly, after noting the value offered by considering multiple bands in FLS detection, a normalized difference fog index was developed in [8] and [16] by analyzing the spectral characteristics of fog and was applied to MODIS data. The authors reported the method performed effectively.

Additionally, a number of studies have taken a different approach for fog detection. As an example, Schulz *et al.* [17] suggested using the pan-sharpened spinning-enhanced visible and infrared imager images instead of using the original channels with 3 km spatial resolution. Similarly, a method based on the principal component analysis, texture analysis, and thresholding was utilized in [18] to detect fog using multifunction transport satellite data. Furthermore, Jasiński *et al.* [7] analyzed various color composites generated from Meteosat second generation and interpreted them in terms of their capability for FLS detection.

There are also a few studies that have developed more complicated approaches to fog detection. In particular, Cermak and Bendix [10] introduced a detailed algorithm for daytime fog detection that included removing the clear-sky and ice cloud pixels and assigning a fog or nonfog class to the remaining pixels. Additionally, National Oceanographic and Atmospheric Administration (NOAA) has developed a comprehensive approach for global fog detection using geostationary operational environmental satellite (GOES) 16 imagery that has been fully described in [19]. In this method, several physical characteristics of fog, such as spatial uniformity and the brightness temperature difference between the cloud and surface and also between the bands centered at 3.9 and 11.2 μm, have been considered. Moreover, several statistical tests were conducted to reduce false alarms [19].

FLS have differences in some applications, such as air and sea navigation, and thus, there are several studies that have the proposed approaches for distinguishing these two meteorological features, such as the article presented in [20]. However, FLS has similar radiation signatures in satellite images [21]. Due to the difficulty in separating fog and low cloud in satellite imagery, they are often referred to as FLS in some studies and they were not separately detected in this study. In this research, an automatic method for daytime sea FLS detection is developed in which the need for the data sources other than the satellite imagery is minimized. The described approach is operational and quick and includes several measures for fog detection. The generated fog map is not binary but presents the probability of sea fog presence for each pixel. Moreover, the proposed method is the first study that utilizes GOES-16 satellite imagery for fog modeling, and the first study that provides a satellite-based solution for detecting fog in Grand Banks, NL. Furthermore, in this study, regional ice-ocean prediction system (RIOPS) data were applied for estimating the relative altitude of the clouds, and NOAA data were used for comparison and validation. The details of the method are provided as follows.
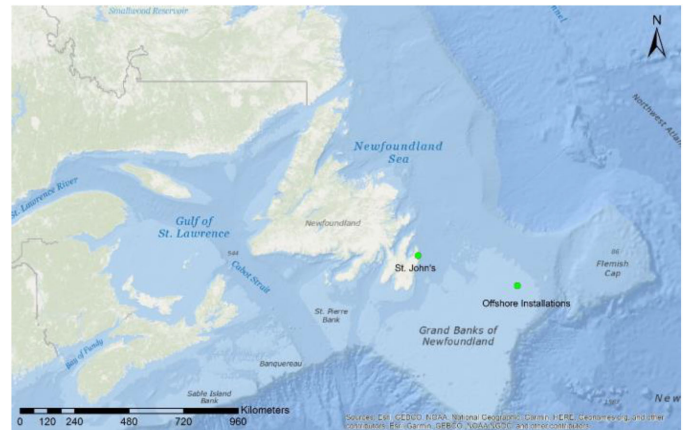

Fig. 1. Study area. The green points are indicative of the capital of NL (St. John's) and the location of the offshore installations where validation was conducted.

II. STUDY AREA AND DATASET

A. Study Area

The study area was the Grand Banks and the surrounding areas of the Newfoundland and Labrador (NL) offshore [22] between the longitudes of 70° W and 45° W, and the latitudes of 40° N and 55° N (see Fig. 1). This area is rich in oil and gas and is the location of several production fields. The NL offshore is characterized by harsh weather that is generally more severe than other offshore oil and gas jurisdictions [23]. This region has relatively sparse meteorological and oceanographic measurement coverage. Intense storms, high winds, cold temperatures, as well as icebergs and sea ice are some of the climatological characteristics of the Grand Banks. Another phenomenon, which is most important to this study, is the frequent occurrence of advection fog in spring and summer because, in this region, the warm moist air over the gulf stream often blows over the colder waters of the Labrador current, creating extensive banks of near zero visibility fog.

B. Datasets

The following categories of data were employed in this study, each of which is briefly described as follows.

1) Satellite Data: GOES-16 advanced baseline imager (ABI) imagery was used in this study. ABI observes the western hemisphere and provides variable radiometric information over this part of the earth [24]. The spectral, spatial, and temporal resolution of ABI are superior to those of comparable sensors on previous GOES satellites [25], providing users with 16 spectral bands, 0.5–2 km spatial resolution, and a 15-min revisit time [24]. Level 2+ GOES-16 data were applied in this study. GOES-16 level 0 data are unprocessed, and when geometric and radiometric corrections are applied on level 0 data, level 1b data are produced. Level 2+ images are obtained by deriving environmental variables from level 1b data as well as several

TABLE I
CHARACTERISTICS OF ABI CHANNELS [24]

Channel #	Central Wavelengths (μm)	Band Type	Used in This Study
1	0.47	Visible	x
2	0.64		x
3	0.86	Near	x
4	1.38	Infrared	
5	1.61		x
6	2.26		
7	3.9	Infrared	x
8	6.15		
9	7.0		
10	7.4		
11	8.5		x
12	9.7		
13	10.35		
14	11.2		
15	12.3		x
16	13.3		

Fig. 2. Flowchart of the method (SZA indicates the solar zenith angle).

ancillary source data [26]. GOES-16 images can be downloaded[1] and the bulk download is available through Amazon S3 and Google Cloud [27]. Table I presents the characteristics of the ABI spectral bands and those that were used in this study.

2) Field Observations: Field data coming from several instruments installed on an offshore platform were used for validating the fog maps. The instruments recorded several surface weather parameters, including wind speed, wind direction, temperature, dew point temperature, relative humidity, and visibility. A Vaisala PWD22 is applied for recording visibility, which can provide the meteorological optical range and present several weather conditions, including visibility, weather intensity, and precipitation. Weather information was recorded as a meteorological aerodrome report (METAR). METAR is a code that has been applied for aviation weather in several parts of the globe since 1996. In Canada, METAR reports are generated by a computer software. METAR reports are generated every hour. Also, when conditions change significantly, a special report (or SPECI) is issued [28]. For selecting the advection fog events, the dates and times during summer 2018 for which the visibility was 0–2 km and the wind direction was 200–250 were selected. Then, the satellite imagery corresponding to these dates and times was checked by a meteorologist to ascertain these times correspond to a fog event. Moreover, several dates and times when there was a clear sky or ice cloud over the offshore installation were selected to see if the proposed algorithm detects these events correctly. Finally, METAR reports for various dates and times of day along with the concurrent satellite images were used for validating the proposed daytime sea FLS detection algorithm.

3) NOAA Visibility Data: NOAA visibility and cloud-type data, accessible through the GEOstationary cloud algorithm testbed, were also employed in this study. The low instrument flight rules (LIFR) condition is defined as a cloud ceiling below 500 ft above the ground level and it is closely related to fog presence. NOAA has generated the LIFR probability map according to the article presented in [19] and the product was
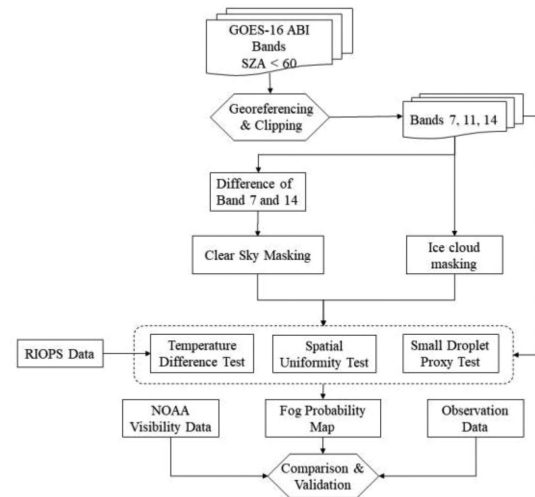
used for comparison with the fog probability maps created in this study. It should be noted that at the time of conducting this study, NOAA products were not fully validated [29].

4) RIOPS Data: In this study, the potential temperature of seawater, representing SST from the RIOPS, was also utilized [30]. The potential temperature of seawater in the RIOPS data is named votemper [30] and was employed for the indirect derivation of cloud height from the satellite imagery. The RIOPS data are provided by the Canadian Centre for Meteorological and Environmental Prediction and presents time-mean ocean forecasts that are interpolated in 5 km spatial resolution and are produced four times a day in 6-h intervals. In [31], the average root-mean-square error of the RIOPS SST was reported to be variable between 0 and 2 °C, depending on the geographical location. In RIOPS data, satellite observations are combined with *in situ* observation [25]. Therefore, RIOPS SST data are preferred over the satellite data alone, which are usually obscured by clouds. This problem of cloud coverage is more severe over the ocean and during a fog event, which is the case in this study.

III. METHOD

Fig. 2 demonstrates the flowchart of the proposed method for the daytime sea fog detection. Initially, the daytime (when the solar zenith angle (SZA) is smaller than 60°) GOES-16 images were georeferenced, and the study area was clipped. Afterward, bands 7, 11, and 14 of the images were used to mask the clear sky and ice clouds and to run different tests to assign a probability of fog to the remaining pixels. Finally, a fog probability map was produced, which was validated using the observation data and NOAA's products. The details of each step are provided in the following sections.

A. Georeferencing and Clipping

In the first step, the required bands of GOES-16 ABI were transferred from the GOES projection to the world geodetic

[1][Online]. Available: https://www.avl.class.noaa.gov/saa/products/welcome
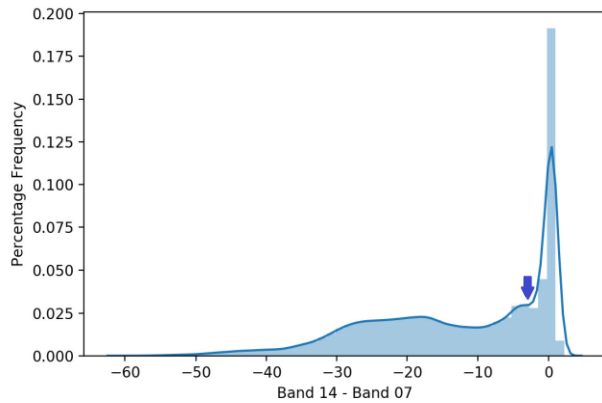
Fig. 3. Distribution of the difference between bands 07 and 14 of GOES-16 for masking the clear-sky areas. The arrow shows the threshold by which the clear-sky areas are masked.

Fig. 4. Example distribution of the difference between the 11.2 μm band brightness temperature and SST represented by RIOPS model data. The arrow shows the location of an observed fog pixel in the histogram.

system 1984 (known as WGS 84) datum using the information available from the image metadata. Afterward, the images were clipped to the area of interest, as described in Section II.

B. Masking Clear Sky

One of the prerequisites of obtaining a sea fog probability map is masking the clear-sky class in the image. To this end, the method described by Cermak and Bendix [10] was used in this study. Since the radiance in the 3.9 μm channel contains both solar and thermal signals, the difference between the 11.2 μm and 3.9 μm channels for a cloud contaminated pixel is greater than that for a cloud-free pixel [10]. Therefore, the distribution of the difference between the brightness temperature of bands 7 and 14 (see Table I) can be considered for masking clear sky [10]. As can be observed in Fig. 3, from right to left, the first local minimum in the histogram after a significant peak was used as a threshold to separate the clear-sky regions. This threshold is determined dynamically, as it is different depending on the viewing geometry and season [10]. However, the same method can be applied to all locations [10].

C. Masking Ice Clouds

Ice fog occurs rarely in any region because it mostly appears when the air temperature is below $-30\,^{\circ}\mathrm{C}$ and there is enough water vapor [19]. Consequently, only the warm fog in the water phase was considered in this study, and ice clouds were masked. When the brightness temperature in band 14 of GOES-16 was below 250 K, an ice cloud was present [10]. Moreover, the difference between bands 11 and 14 was applied to remove thin cirrus clouds. When the brightness temperature of band 11 exceeds that of band 14, a thin cirrus cloud was probably present [10].

D. Generation of the Fog Probability Map

The sea fog probability map was produced using three different metrics. The final fog probability map was gained by averaging all three yielded maps.
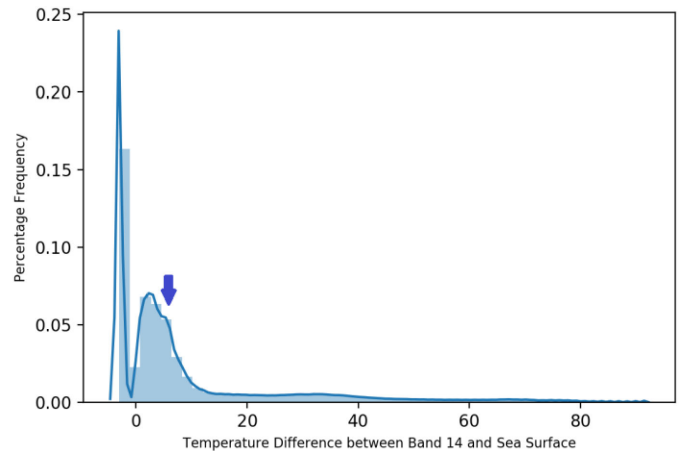
1) Temperature Difference Test: The difference between the cloud and SST has a direct relationship with cloud height. Therefore, the smaller this difference is, the more probable it is that fog occurs [19]. Cloud temperature in 11.2 μm is available in band 14 of GOES-16. For SST, RIOPS near-surface modeled temperature was used for estimating cloud altitude [30]. However, it should be noted that several other methods can be used for this purpose. For example, Cermak and Bendix [10] used the difference between the temperature of the cloud and a near clear-sky area for estimating the cloud altitude. As another example, Calvert and Pavolonis [19] obtained surface temperature using several ancillary parameters, such as surface emissivity, atmospheric transmittance, and atmospheric radiance. There are also multihourly or daily SST products derived from satellite data, but those are not available in real time due to the significant cloud coverage in optical images, especially over the Grand Banks ocean environment. Therefore, modeled SST data were used in the current study for estimating cloud altitude.

The difference between the brightness temperature in band 14 and the RIOPS surface temperature was utilized to produce a fog probability map. Fig. 4 demonstrates an example of the distribution of the difference between the 11.2 μm brightness temperature and the modeled surface temperature for July 17, 2018, 11:00 A.M. The arrow demonstrates the location of a foggy pixel, confirmed with observation, having approximately 6° of difference with the ocean surface. As the temperature difference between the cloud and the surface increases for a pixel, there is a lower chance for the fog presence.

2) Spatial Uniformity Test: Generally, the fog has more spatial uniformity compared with clouds [10], [19]. Consequently, the standard deviation of band 14 was computed, and higher probabilities were assigned to smaller values of standard deviation. It should be noted that this fact is not location dependent and can be applied in any desired area. Fig. 5 demonstrates an example distribution of the standard deviations in 3 × 3 windows centered on each pixel. As can be observed, the observed fog pixel indicated by an arrow has a very small standard deviation.
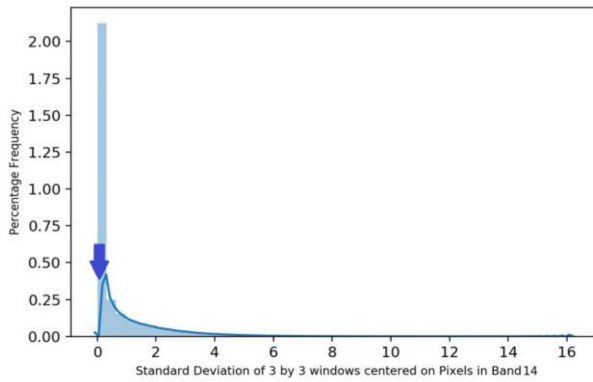
Fig. 5. Example of the distribution of the standard deviations in 3×3 windows centered on pixels. The arrow shows the location of an observed fog pixel in the histogram.
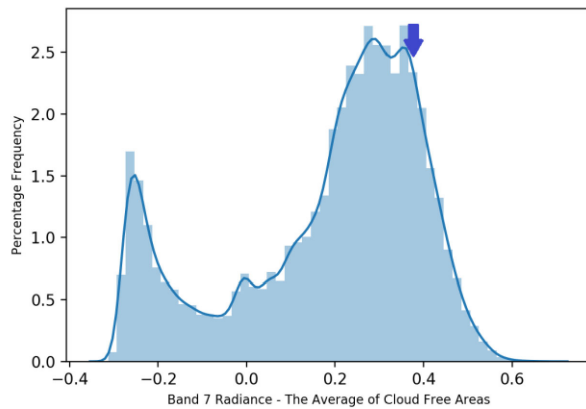

Fig. 6. Distribution of the difference between the pixel radiance in 3.9 μm and the average of clear-sky radiance in the same channel. The arrow shows the location of an observed fog pixel in the histogram.

3) Small Droplet Proxy Test: Fog and low clouds contain small droplets that are slightly reflective at the 3.9 μm channel [32]. Consequently, the radiance received from FLS exceeds that from clear-sky areas and other types of cloud. This property can be applied for fog detection. The 3.9 μm radiance, corresponding to band 7 of GOES-16, was averaged over clear-sky areas at almost the same latitude [10]. Afterward, fog probabilities were assigned to the pixels in accordance with the difference between the band 7 radiance in a cloudy pixel and the obtained latitudinal average value. Then, a higher probability of fog is assigned to the pixels having greater temperature difference with clear-sky area at the same latitude. Fig. 6 demonstrates an example distribution of the difference between band 7 radiance and the average of cloud-free pixels in the same channel. The arrow demonstrates a foggy pixel, confirmed by field observation, which has a relatively high-temperature difference with the clear-sky areas. The pixels having more temperature difference than the shown pixel are assigned a higher fog probability in the algorithm.

It should be noted that although Figs. 4–6 show an example distribution, the distributions for other dates and times are similar to the depicted figures. Each pixel, which is not masked as the

clear sky or ice cloud, is given a probability based on its location in the distributions corresponding to three tests described above. Therefore, no threshold is used to separate fog or nonfog events at this point and only a probability is computed. When the final fog probability map is produced, it will be thresholded in different probability values, as demonstrated in Section IV.

E. Comparison and Validation

When the final fog probability maps were created, they were validated in various ways. First, the corresponding pseudotrue color composites were created. For the visual inspection of the fog probability maps, it was necessary to generate a true color composite image. For this, the red, green, and blue bands are required. However, GOES-16 lacks a green band [24]. Therefore, as elaborated in [33] and demonstrated in (1), a linear relationship using bands 1–3 of GOES-16 was developed to derive the reflectance of the green band

$$B_{\text{Green}} = 0.45706946\, B_1 + 0.48358168\, B_2 + 0.06038137\, B_3 \tag{1}$$

where B_{Green} is the pseudogreen band, and B_i represents the ith bands of GOES-16. The three bands were subsequently stacked to produce a pseudotrue color composite. The fog probability maps were visually investigated in a case study, as was described in Section IV.

Second, several measures (described in the following) were used to validate the fog maps statistically.

For probability-based accuracy assessment, an index was introduced in this study, which was called the average detection probability (ADP), and was computed as the average of the probabilities assigned to the pixels at the location and time corresponding to which was detected as fog by field observations.

If false positives, false negatives, true positives, and true negatives are indicated with FP, FN, TP, and TN, respectively, false alarm rate (FAR), probability of detection (POD), critical success index (CSI), percentage error (ERR), and hit rate (HR) are defined as follows [4]:

$$\text{FAR} = \frac{\text{FP}}{\text{TN} + \text{FP}} \tag{2}$$

$$\text{POD} = \frac{\text{TP}}{\text{TP} + \text{FN}} \tag{3}$$

$$\text{CSI} = \frac{\text{TP}}{\text{TP} + \text{FP} + \text{FN}} \tag{4}$$

$$\text{ERR} = \frac{\text{FN} + \text{FP}}{\text{TP} + \text{TN} + \text{FP} + \text{FN}} \tag{5}$$

$$\text{HR} = 1 - \text{ERR}. \tag{6}$$

Another useful measure for evaluating the performance of the algorithm is Hanssen–Kuiper skill score (KSS) [5], which is computed as

$$\text{KSS} = \text{POD} - \text{FAR} \tag{7}$$

which has a range from -1 to 1. Positive (negative) values for KSS indicate a positive (negative) correlation between the map

and the observations. It should be noted that the indices described above are for a binary map. Therefore, to apply them to the maps generated in this study, these maps should be thresholded to change them from a probability-based map, including all the numbers in the range [0,1] to the maps that only include {0,1} numbers. For this purpose, several thresholds {0.2, 0., 0.6, 0.65, and 0.70} were selected based on all of which the maps were binarized and the above metrics were computed. Moreover, the results were compared with NOAA's visibility and cloud-type products in both validation steps.

IV. RESULTS AND DISCUSSION

The color composites and the probability-based sea fog maps were generated using the elaborated algorithm in Section III. The fog maps were evaluated and discussed both visually during a fog event and using several statistical metrics after binarization. Moreover, a comparison with NOAA's products was provided in each step. The details of each process are described in the following sections.

A. Demonstration of an Advection Fog Event

Initially, three images with an acquisition time interval of 1 h that represented an advection fog event occurring on July 17, 2018, from 13:00 to 15:00 of universal time coordinated were selected and processed. According to the METAR data, the wind speed was 45 knots and the temperature was about 15 °C at the offshore platform during the time of the event. Moreover, horizontal visibility was recorded as 0 km and the low cloud cover percentage and height were 100% and 200 ft above the sea level, respectively, at this location. This fog event occurred because of the advection of warm moist air originating from over the Gulf Stream passing over colder waters originating from the Labrador current, which caused the air to cool below its dew point and condense into fog droplets.

Fig. 7 represents the pseudotrue color composites along with the corresponding fog probability maps. The pseudocolor composites created in this study, despite the lack of green band in the GOES-16 image, can assist in both the visual assessment of the fog maps as well as the detection of various meteorological phenomena. In the probability-based fog map, the land was masked for two reasons: First, detecting fog events over the land was not within the project scope; second, the land surface temperature was not available as accurately and timely as the SST data at the time of the study. Other than the fog probability, the maps include the clear-sky and ice cloud classes. The accurate delineation of these two classes was important because only the remaining areas were assigned probability. Therefore, if a foggy area was mistakenly included in one of these classes, it could not be detected in the final fog probability map. In fact, one of the challenges in the current study was that the accuracy of the clear-sky and ice classes directly affected the fog detection accuracy. Therefore, it was very important to increase the accuracy of these two classes along with boosting the accuracy of the fog detection algorithm.

Clear-sky areas can be verified by comparing the color composites with the probability maps. By doing so, it was observed

that most clear-sky areas were identified accurately with a slight overestimation at some locations, which caused a few small fog events to be missed. Moreover, a haze layer can be seen in Fig. 7(a) between the longitudes of 65 °W and 60 °W and the latitudes of 45 °N and 50 °N, which was mostly detected as clear sky. In this study, ice clouds could not be verified by the visual assessment of the color composite or by field observation. However, the areas detected as ice cloud in Fig. 7(b), (d), and (f) were also detected as ice clouds in NOAA's cloud-type product, as depicted in Fig. 7(a), (c), and (e), although an underestimation occurred if it is assumed that NOAA's cloud-type product was accurate.

In all three maps, as provided in Fig. 7, the fog was identified with a high probability over the offshore platform, which showed the accurate performance of the algorithm. A marine meteorologist expert confirmed that most advection fog areas were identified with a high probability.

1) Comparison With NOAA's Products: Fig. 8 demonstrates NOAA's cloud-type product along with its corresponding LIFR maps. By comparing with the color composite images, as depicted in Fig. 7, most clear-sky areas were identified correctly in the NOAA's cloud-type product and were assigned zero or very low LIFR probabilities, although it showed slight underestimation. Moreover, this product failed to completely detect the previously described haze event as well. The other cloud types cannot be verified visually, but the region detected as ice cloud conformed to the ice cloud classes in Fig. 7(b), (d), and (f). However, certain differences exist, and several more ice cloud patches were detected using the NOAA's products, which were not detected using the proposed method.

In the NOAA's fog probability map, as represented in Fig. 8(b), (d), and (f), fog probability was zero or very low over the offshore platform, which means that this algorithm failed to successfully detect the fog event at this location. This was also true for the surrounding regions with similar spectral characteristics. Furthermore, the region detected as ice cloud by NOAA's algorithm was assigned a high fog probability, while ice fogs occur very rarely [19]. Although fog could occur below the ice cloud, remote sensing (RS) is unable to detect such a fog event by penetrating through the clouds. Additionally, certain discontinuities can be seen in the fog map produced by NOAA [e.g., Fig. 8(b)] between the longitudes of 50°W and 45°W and the latitudes of 45°N and 50°N, which show some limitations of the algorithm.

B. Statistical Evaluation of the Fog Maps

Table II presents the fog and nonfog events selected for the validation of the proposed method. Initially, the probability-based fog maps were assessed using the ADP index with the fog events, as given in Table II. ADP for the generated fog maps was 65.87%, which means that, on average, a real advection fog event was detected with the probability of approximately 66% using the proposed algorithm. Therefore, a probability close to but below this value (e.g., 60%) should be an appropriate rate at which the fog map is binarized. The same value for the NOAA LIFR map was 37.97%. Fig. 9 demonstrates a comparison between
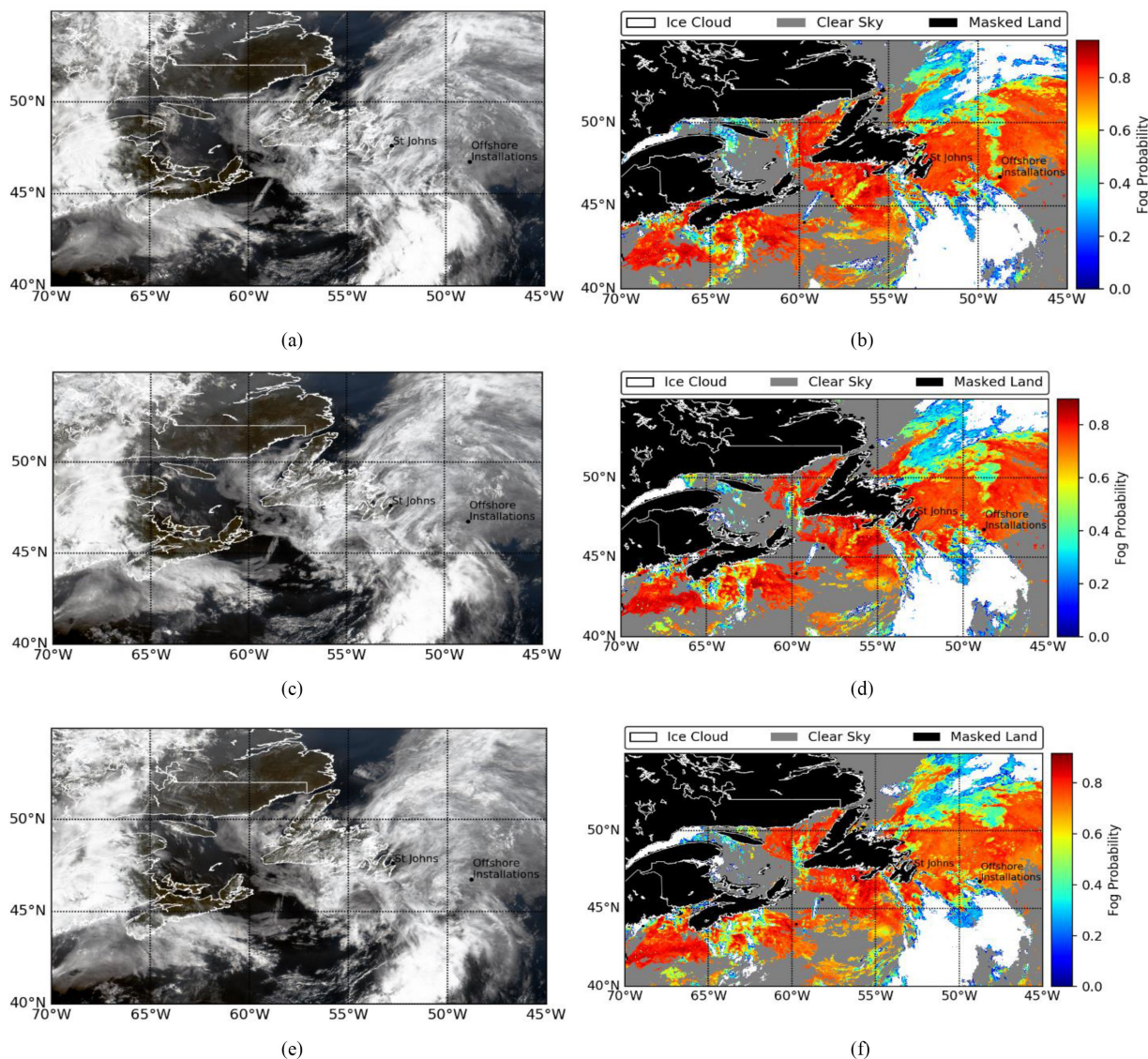
Fig. 7. Pseudocolor composites (left column) and the corresponding probability-based fog maps (right column). (a) 2018-07-17- 13:00. (b) 2018-07-17- 13:00. (c) 2018-07-17- 14:00. (d) 2018-07-17- 14:00. (e) 2018-07-17- 15:00. (f) 2018-07-17- 15:00.

the probabilities obtained by the proposed method and those provided by NOAA for the observed advection fog events. For the proposed method, approximately 78% of the advection fog events were detected with probabilities greater than 60% and only 12% of the detection probabilities laid below 40%. However, for the NOAA maps, 87% of the advection fog events were detected with a probability of less than 60%, and most of the events were identified with the probabilities of 21%–40%.

The next step was to evaluate the deterministic fog maps using field observations. For this purpose, initially, the METAR reports for the months of July and August 2018, when the most advection fog events occur, were investigated and the METAR observations reporting advection sea fog events were selected. However, as mentioned before, one of the RS limitations in this regard is that fog cannot be detected when the cloud is present above the fog layer, as optical imagery is unable to penetrate through the clouds. Therefore, the observations that

were identified as ice cloud by the proposed algorithm were separated. The remaining observations, showing the fog events, are depicted on the left side of Table II. For these observations, the fog probability of the pixel corresponding to the observation location was evaluated for the accuracy assessment, which was zero if the pixel was detected as a clear sky.

Furthermore, the maps were evaluated in terms of TNs or FPs. Therefore, several ice cloud and clear-sky events were selected for examination, as shown on the right side of Table II. For these events, a comparison of the true color composite with NOAA's cloud-type product was made to see if the ice cloud/clear-sky events were detected correctly or if a false fog event was reported. Few clear-sky events were found over the offshore platform, most of which were identified correctly. Occasionally, however, clear-sky areas over a random point were identified as fog with a high certainty that caused a constant FAR as the threshold varies (see Table III).
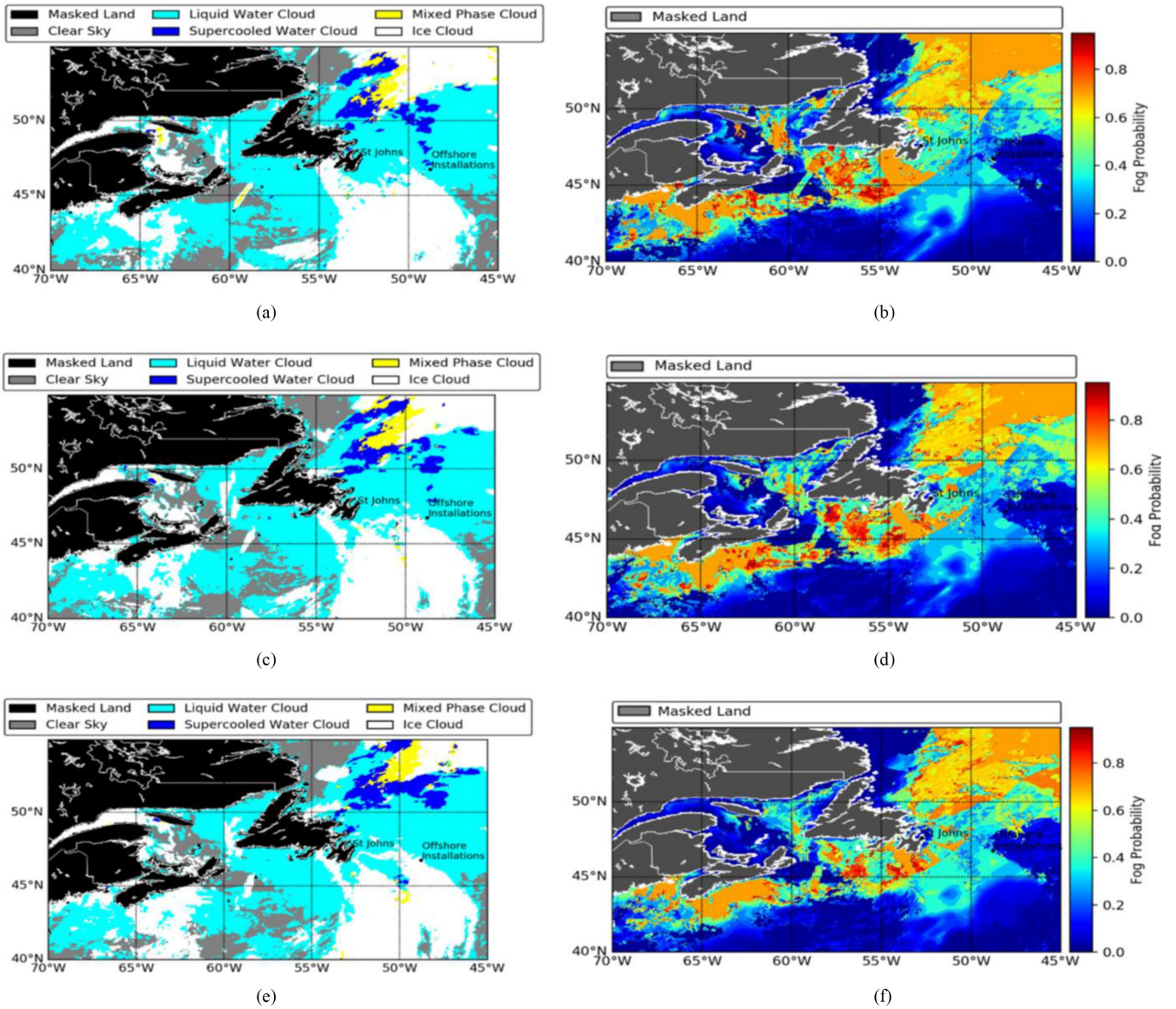
Fig. 8. NOAA's cloud-type product (left column) and the corresponding NOAA's LIFR map (right column). (a) 2018-07-17- 13:00. (b) 2018-07-17- 13:00. (c) 2018-07-17- 14:00. (d) 2018-07-17- 14:00. (e) 2018-07-17- 15:00. (f) 2018-07-17- 15:00.
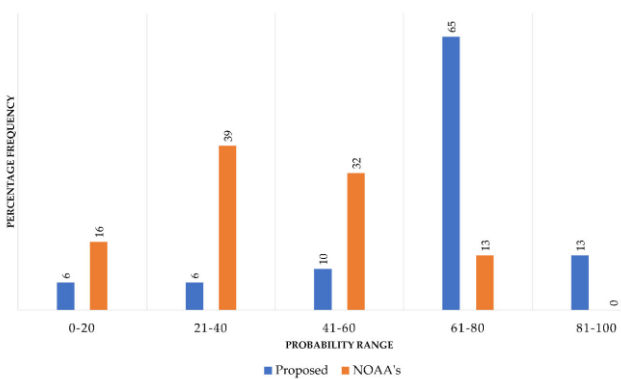

Fig. 9. Comparison of the probabilities obtained by the proposed method and NOAA's algorithm for the observed advection fog events.

As expected, POD decreased as the binarization probability increased. The 60% binarization probability, as a reasonable binarization probability for the produced maps, yielded a POD of 0.77, which means that 77% of the advection fog events were detected with a probability greater than 60%. CSI was slightly lower than POD because both FPs and FNs were considered in this index. This value was 0.73 for the map with a 60% binarization probability. For the same map, ERR and HR, which are complementary to each other, were 0.17 and 0.83, respectively, which represent a rather high HR for the produced map. Finally, the KSS value for this map indicates that there was a 0.68 correlation between the produced map and the field observations.

TABLE II
FOG AND NONFOG EVENTS SELECTED FOR VALIDATION OF THE
PROPOSED METHOD

Fog events			Non-fog events		
Dates	Value in the generated map	Value in the NOAA map	Dates	Value in the generated map	True Color Composite image and NOAA product
7/2/2018 15:00	61	3	7/1/2018 15:00	Ice Cloud	Ice Cloud
7/3/2018 18:00	35	37	7/5/2018 15:00	Clear Sky	Clear Sky
7/3/2018 19:00	71	40	7/8/2018 15:00	Clear Sky	Clear Sky
7/3/2018 21:00	71	73	7/15/2018 21:00	Ice Cloud	Ice Cloud
7/4/2018 15:00	76	40	7/16/2018 18:00	Ice Cloud	Ice Cloud
7/10/2018 16:00	77	54	7/16/2018 19:00	Ice Cloud	Ice Cloud
7/10/2018 17:00	76	33	7/19/2018 15:00	Ice Cloud	Ice Cloud
7/10/2018 18:00	79	43	7/19/2018 16:00	Ice Cloud	Ice Cloud
7/10/2018 19:00	78	43	7/19/2018 18:00	Ice Cloud	Ice Cloud
7/10/2018 21:00	73	54	7/20/2018 15:00	Ice Cloud	Ice Cloud
7/11/2018 15:00	77	41	7/20/2018 18:00	Ice Cloud	Ice Cloud
7/11/2018 16:00	78	14	7/23/2018 18:00	Ice Cloud	Ice Cloud
7/11/2018 17:00	79	42	8/1/2018 15:00	Clear Sky	Clear Sky
7/12/2018 15:00	71	45	8/1/2018 18:00	Clear Sky	Clear Sky
7/12/2018 16:00	58	18	8/2/2018 15:00	Clear Sky	Clear Sky
7/12/2018 17:00	82	35	8/2/2018 18:00	Clear Sky	Clear Sky
7/12/2018 18:00	80	33	8/5/2018 15:00	75	Clear Sky
7/15/2018 15:00	20	23	8/7/2018 15:00	75	Clear Sky
7/16/2018 16:00	79	5	8/11/2018 15:00	Ice Cloud	Ice Cloud
7/16/2018 17:00	47	30	8/13/2018 15:00	Clear Sky	Clear Sky
7/17/2018 15:00	46	37	8/24/2018 15:00	Ice Cloud	Ice Cloud
7/17/2018 19:00	61	32	8/30/2018 19:00	Clear Sky	Clear Sky
7/17/2018 21:00	73	52			
7/18/2018 15:00	0	6			
7/18/2018 18:00	85	34			
7/23/2018 15:00	80	41			
8/3/2018 15:00	30	70			
8/3/2018 18:00	81	66			
8/22/2018 18:00	86	44			
8/23/2018 15:00	70	74			
8/24/2018 21:00	62	37			

TABLE III
SEVERAL METRICS FOR EVALUATING THE GENERATED FOG
PROBABILITY MAPS

	P >= 20%	P >= 40%	P >= 60%	P >= 65%	P >= 70%
FAR	0.09	0.09	0.09	0.09	0.09
POD	0.97	0.87	0.77	0.68	0.68
CSI	0.91	0.82	0.73	0.64	0.64
ERR	0.06	0.11	0.17	0.23	0.23
HR	0.94	0.89	0.83	0.77	0.77
KSS	0.88	0.78	0.68	0.59	0.59

Note: $P> = x\%$ means that the probability-based map has been binarized on the probability of $x\%$.

C. Uncertainties

Finally, it should be noted that, as with any novel technique, the current validation method has some limitations that should be considered when it is applied. As the title of the article indicates, this method should be applied during daytime only (i.e., when the SZA is smaller than 60°), and the accuracy is affected during dawn/dusk or nighttime.

Another item to consider is the distribution of field data. For this study, field data were available only over the offshore station. Although spatial accuracy assessment was conducted over the whole region by a marine meteorological expert and using NOAA's products, it should be noted that the statistical assessment was conducted only over given points. Moreover, from the time aspect, the validation was conducted during July and August. Although the peak advection fog season for the study area is from June to August, this limitation should be considered when applying the method.

There are other meteorological phenomena, such as light rain, which may look similar to fog in some type of images. One of the valuable works in the future could be the detection of rain using radar data, using methods similar to what is described in [34] and [35].

V. CONCLUSION

In this article, a probability-based algorithm was introduced for daytime sea fog detection that utilizes GOES-16 images and modeled SST data. First, pseudocolor composites were generated by interpolating green band using the first three bands of GOES-16. Then, the probability-based fog maps were produced. For this purpose, clear-sky and ice cloud areas were initially delineated, and then three tests of small droplet proxy, spatial homogeneity, and temperature difference were conducted on the remaining pixels to assign a fog probability to each. The probability-based sea fog maps were visually assessed during an advection fog event in July 2018. Generally, the clear-sky areas were detected with a high accuracy but were slightly overestimated. Ice cloud regions had good agreement with NOAA's cloud-type product, and high probabilities had been assigned to the pixels corresponding to the location of observed advection fog events. Using the proposed algorithm, the ADP for observed fog events was approximately 66%, while the same value for the NOAA's LIFR maps was about 38%. Moreover, by using 60% threshold value, FAR, POD, HR, and KSS were 0.09, 0.77, 0.73,

and 0.68, respectively. Therefore, the proposed algorithm has the potential to detect sea fog in the Grand Banks region with a high confidence and can potentially improve offshore vessel and air navigation.

REFERENCES

[1] J. Deng, J. Bai, J. Liu, X. W. Wang, and H. Y. Shi, "Detection of daytime fog using MODIS multispectral data," *Meteorol. Sci. Technol.*, vol. 34, no. 2, pp. 188–193, 2006.

[2] Y.-J. Deng, J.-C. Wang, J. Cao, and C.-X. Cao, "Detection of daytime fog in South China sea using MODIS data," *J. Tropical Meteorol.*, vol. 20, no. 4, pp. 386–390, 2014.

[3] S. Chaurasia and B. S. Gohil, "Detection of day time fog over India using INSAT-3D data," *IEEE J. Sel. Topics Appl. Earth Obs. Remote Sens.*, vol. 8, no. 9, pp. 4524–4530, Sep. 2015.

[4] J. Bendix, B. Thies, J. Cermak, and T. Nauß, "Ground fog detection from space based on MODIS daytime data—A feasibility study," *Weather Forecast.*, vol. 20, no. 6, pp. 989–1005, 2005.

[5] X. Wu and S. Li, "Automatic sea fog detection over Chinese adjacent oceans using Terra/MODIS data," *Int. J. Remote Sens.*, vol. 35, no. 21, pp. 7430–7457, 2014.

[6] I. Gultepe *et al.*, "Fog research: A review of past achievements and future perspectives," *Pure Appl. Geophys.*, vol. 164, no. 6/7, pp. 1121–1159, 2007.

[7] J. Jasiński, K. Krawczyk, and S. Pietrek, "Fog detection over sea based on multispectral analysis of satellite images," *Zesz. Nauk. Morska w Szczecinie*, vol. 29, no. 101, pp. 53–62, 2012. [Online]. Available: http://yadda.icm.edu.pl/baztech/element/bwmeta1.element.baztech-article-BWM6-0028-0009

[8] X. Wen *et al.*, "An object-oriented daytime land fog detection approach based on NDFI and fractal dimension using EOS/MODIS data," *Int. J. Remote Sens.*, vol. 35, no. 13, pp. 4865–4880, 2014.

[9] S. Zhang and L. Yi, "A comprehensive dynamic threshold algorithm for daytime sea fog retrieval over the Chinese adjacent seas," *Pure Appl. Geophys.*, vol. 170, no. 11, pp. 1931–1944, 2013.

[10] J. Cermak and J. Bendix, "A novel approach to fog/low stratus detection using Meteosat 8 data," *Atmos. Res.*, vol. 87, no. 3/4, pp. 279–292, 2008.

[11] M. Amani, S. Mahdavi, T. Bullock, and S. Beale, "Automatic nighttime sea fog detection using GOES-16 imagery," *Atmos. Res.*, vol. 238, 2020, Art. no. 104712.

[12] S. Dehnavi, Y. Maghsoudi, K. Zakšek, M. J. V. Zoej, G. Seckmeyer, and V. Skripachev, "Cloud detection based on high resolution stereo pairs of the geostationary Meteosat images," *Remote Sens.*, vol. 12, no. 3, 2020, Art. no. 371.

[13] J. Bendix, J. Cermak, and B. Thies, "New perspectives in remote sensing of fog and low stratus-TERRA/AQUA-MODIS and MSG," in *Proc. 3rd Int. Conf. Fog, Fog Collection Dew*, Cape Town, South Africa, 2004, vol. 11, pp. 11–15.

[14] J. J. Gurka, "Using satellite data for forecasting fog and stratus dissipation," in *Proc. 5th Conf. Weather Forecast. Anal.*, St. Louis, MO, USA, 1974, pp. 54–57.

[15] M. Huiyun and W. Zhao, "A daytime radiation fog detecting scheme based on TERRA/MODIS data over land," in *Proc. 2nd Int. Workshop Educ. Technol. Comput. Sci.*, 2010, pp. 299–302.

[16] L. Liu *et al.*, "An object-oriented daytime land-fog-detection approach based on the mean-shift and full lambda-schedule algorithms using EOS/MODIS data," *Int. J. Remote Sens.*, vol. 32, no. 17, pp. 4769–4785, 2011.

[17] H. M. Schulz, B. Thies, J. Cermak, and J. Bendix, "1 km fog and low stratus detection using pan-sharpened MSG SEVIRI data," *Atmos. Meas. Techn.*, vol. 5, no. 10, pp. 2469–2480, 2012.

[18] L. Jun, H. Zhi-Gang, C. Hong-Bin, Z. Zeng-Liang, and W. Hong-Yi, "Fog detection over China's adjacent sea area by using the MTSAT geostationary satellite data," *Atmos. Ocean. Sci. Lett.*, vol. 5, no. 2, pp. 128–133, 2012.

[19] C. Calvert and M. Pavolonis, "GOES-R advanced baseline imager (ABI) algorithm theoretical basis document for low cloud and fog," Space Sci. Eng. Center, Univ. Wisconsin—Madison, Madison, WI, USA, 2010.

[20] M. Weston and M. Temimi, "Application of a nighttime fog detection method using SEVIRI over an arid environment," *Remote Sens.*, vol. 12, no. 14, 2020, Art. no. 2281.

[21] J. Cermak, R. M. Eastman, J. Bendix, and S. G. Warren, "European climatology of fog and low stratus based on geostationary satellite observations," *Quart. J. Roy. Meteorol. Soc.*, vol. 135, no. 645, pp. 2125–2130, 2009.

[22] T. Bullock, G. A. Isaac, J. Beale, and T. Hauser, "Improvement of visibility and severe sea state forecasting on the grand banks of Newfoundland and Labrador," in *Proc. Arctic Technol. Conf.*, 2016. [Online]. Available: https://doi.org/10.4043/27406-MS

[23] *Petroleum and Natural Gas Industries—Specific Requirements for Offshore Structures—Part 4: Geotechnical and Foundation Design Considerations*, ISO: 19901-4, 2003.

[24] GOES-R Ser. Program Office, "Instruments: Advanced baseline imager (ABI)," Nat. Ocean. Atmos. Admin., 2018. [Online]. Available: https://www.goes-r.gov/spacesegment/abi.html

[25] D. T. Lindsey, D. Bikos, and L. Grasso, "Using the GOES-16 split window difference to detect a boundary prior to cloud formation," *Bull. Amer. Meteorol. Soc.*, vol. 99, no. 8, pp. 1541–1544, 2018.

[26] "GOES-R product processing," Nat. Ocean. Atmos. Admin., Accessed: Jan. 2019. [Online]. Available: https://noaasis.noaa.gov/GOES/goes-r_product_processing.html

[27] "NOAA GOES-R series advanced baseline imager (ABI) level 2 cloud and moisture imagery products (CMIP)," Nat. Ocean. Atmos. Admin., 2020. [Online]. Available: https://data.nodc.noaa.gov/cgi-bin/iso?id=gov.noaa.ncdc:C01502

[28] I. O. F. D. O. F. M. visibility, "Aerodrome meteorological observation and forecast study group (AMOFSG)." Accessed: Mar. 2019. [Online]. Available: https://mediawiki.ivao.aero/index.php?title=METAR_explanation

[29] NOAA NESDIS OSPO, "GOES user information and documents," Nat. Ocean. Atmos. Admin., 2018. Accessed: Jan. 10, 2018. [Online]. Available: https://www.ospo.noaa.gov/Operations/GOES/documents.html

[30] Meterol. Service Canada, "RIOPS data description," in *Environment and Climate Change Canada*, 2018. Accessed: Dec. 10, 2018. [Online]. Available: http://dd.alpha.meteo.gc.ca/yopp/model_riops/doc/README_RIOPS.txt

[31] G. C. Smith *et al.*, "The regional ice ocean prediction system v2: A pan-Canadian ocean analysis system," Geoscientific Model Development Discussions, 1–49, 2020. [Online]. Available: https://doi.org/10.5194/gmd-2020-255

[32] G. E. Hunt, "Radiative properties of terrestrial clouds at visible and infrared thermal window wavelengths," *Quart. J. Roy. Meteorol. Soc.*, vol. 99, no. 420, pp. 346–369, 1973.

[33] Open Commons Consortium, "Using Python to explore GOES-16 data," 2018. [Online]. Available: https://unidata.github.io/python-gallery/examples/mapping_GOES16_TrueColor.html

[34] X. Chen and W. Huang, "Identification of rain and low-backscatter regions in X-band marine radar images: An unsupervised approach," *IEEE Trans. Geosci. Remote Sens.*, vol. 58, no. 6, pp. 4225–4236, Jun. 2020.

[35] X. Chen, W. Huang, C. Zhao, and Y. Tian, "Rain detection from X-band marine radar images: A support vector machine-based approach," *IEEE Trans. Geosci. Remote Sens.*, vol. 58, no. 3, pp. 2115–2123, Mar. 2020.

Sahel Mahdavi received the Ph.D. degree in electrical engineering from the Memorial University of Newfoundland, St. John's, NL, Canada, in 2018.

Having almost ten years of academic and industrial background in remote sensing, she is familiar with a wide array of topics relevant to RS/GIS and their applications in various environmental aspects. These topics include object-based wetland classification using a combination of optical and full-polarimetric SAR data, feature selection, soil moisture retrieval using SAR images, image segmentation, speckle reduction in SAR images, target detection in multispectral optical images, and the relationship between the environmental conditions and SAR images. She also coauthored a book entitled *Principles of SAR Remote Sensing* and has authored more than 40 peer-reviewed journals. She was a member of a provincial project on wetland classification during her Ph.D. when she identified the problem with wetland classification using remote sensing and, subsequently, proposed a novel scheme for wetland mapping. He is currently affiliated with the data analytics team with Wood PLC, Aberdeen, U.K.

Dr. Mahdavi was a recipient of the Professional Engineers and Geoscientists Newfoundland and Labrador Environmental Award, in 2020, the Emera Graduate Scholarship for Distinctive Women in Engineering for three consecutive years from 2016 to 2018, and the Newfoundland and Labrador Branch of the Canadian Institute of Geomatics Scholarship, in 2015.

Meisam Amani (Senior Member, IEEE) received the B.Eng. degree in geomatics engineering from the University of Tabriz, Tabriz, Iran, in 2012, the M.Eng. degree in remote sensing engineering from the K.N. Toosi University of Technology, Tehran, Iran, in 2014, and the Ph.D. degree in electrical engineering from the Memorial University of Newfoundland, St. John's, NL, Canada, in 2018.

He is currently a Senior Remote Sensing Engineer and the Key Specialty Leader of data analytics with a global consulting and engineering company, called Wood PLC, Aberdeen, U.K., where he manages and leads various industrial, governmental, and academic remote sensing projects worldwide. Over the past 11 years, he has worked on different applications of remote sensing, including but not limited to land cover/land use classification, soil moisture estimation, drought monitoring, water quality assessment, watershed management, power/transmission line monitoring, fog detection and nowcasting, and ocean wind estimation. To do these, he has utilized various remote sensing datasets (e.g., UAV, optical, LiDAR, SAR, scatterometer, radiometer, and altimeter) along with different machine learning and big data processing algorithms.

Dr. Amani was a recipient of the prestigious Professional Engineers and Geoscientists Newfoundland and Labrador Environmental Award, in 2020 due to his contribution to wetland mapping in Canada using advanced machine learning and big data processing algorithms. A list of his research works, including over 50 peer-reviewed journal and conference papers, can be found at https://www.researchgate.net/profile/Meisam_Amani3. He is an Associate Editor for IEEE JOURNAL OF SELECTED TOPICS IN APPLIED EARTH OBSERVATIONS AND REMOTE SENSING and the Lead Guest Editor for a special issue in the *Remote Sensing* journal. He also serves as a regular reviewer in about 15 international remote sensing journals.

Terry Bullock received the B.Sc. degree in physics from St. Mary's University, Nova Scotia, Canada, in 1984, and the Diploma in meteorology from Dalhousie University, Nova Scotia, Canada, in 1985.

He is a Senior Physical Environmental Scientist with some 35 years of operational and research experience in Canada and internationally. He was a Professional Meteorologist providing operational and consultative meteorological and oceanographic services to industrial and government clients. He has been working as a Consulting Marine Meteorologist, since 1985 and specializes in on-site support for environmentally sensitive projects, such as heavy lift operations; wind energy resource monitoring and assessment, and regulatory compliance. Projects include on-site weather support for the construction and installation of the world's most massive oil installation (Hibernia), construction of the White Rose FPSO, construction of the Sable Island offshore energy project, and provision of physical environmental monitoring and forecasting services for the multibillion-dollar Hebron project. His research and development activities include wind boundary layer modeling, wind turbine energy potential and site assessment, marine and terrestrial climatological analysis, extreme event analysis, atmospheric mass and wind analysis, real-time data assimilation into analysis and forecasting systems, dynamical and statistical met-ocean-ice modeling, and weather-observation data processing and quality control. He is the client representative for several offshore operational metocean programs, and has been a Principal Investigator for multiyear R&D projects, and is the Wood Meteorological and Oceanographic Services Key Specialty Lead.
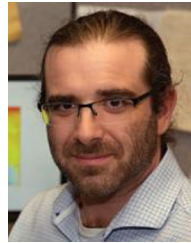
Steven Beale received the B.Sc. degree in physics from Simon Fraser University, Vancouver, BC, Canada, in 2004, and the Ph.D. degree in physics from York University, Toronto, ON, Canada, in 2010.

He is a Senior Data Scientist/Engineer developing and deploying predictive meteorological models with Wood. He has worked in particle physics with both the D0 and ATLAS collaborations. His current work is focused primarily on the design and development of data pipelines for meteorological forecast data and remote sensing data and the automation of predictive models using that pipeline.